AGU PUBLICATIONS

JGR

Journal of Geophysical Research: Solid Earth

RESEARCH ARTICLE

10.1002/2015JB012165

Distributed fault slip model for the 2011 Tohoku-Oki earthquake from GNSS and GRACE/GOCE satellite gravimetry

Martin Johann Fuchs[1], Andrew Hooper[2], Taco Broerse[3], and Johannes Bouman[1]

[1]German Geodetic Research Institute, Technical University of Munich, Munich, Germany, [2]School of Earth and Environment, University of Leeds, Leeds, UK, [3]Department of Geoscience and Remote Sensing, Delft University of Technology, Delft, Netherlands

Key Points:

- Distributed fault slip model from GNSS and GRACE/GOCE satellite gravimetry
- 2011 Tohoku-Oki earthquake coseismic and postseismic change
- Improvements in fault slip modeling due to fine-scale gravity data

Supporting Information:

- Text S1
- Text S2

Correspondence to:
M. J. Fuchs,
martin.fuchs@tum.de

Citation:
Fuchs, M. J., A. Hooper, T. Broerse, and J. Bouman (2016), Distributed fault slip model for the 2011 Tohoku-Oki earthquake from GNSS and GRACE/GOCE satellite gravimetry, *J. Geophys. Res. Solid Earth*, *121*, 1114–1130, doi:10.1002/2015JB012165.

Received 2 MAY 2015
Accepted 24 DEC 2015

Abstract The Gravity Recovery and Climate Experiment (GRACE) mission (launched 2002) and the Gravity Field and Steady-State Ocean Circulation Explorer (GOCE) mission (March 2009 to November 2013) collected spaceborne gravity data for the preseismic and postseismic periods of the 2011 Tohoku-Oki earthquake. In addition, the dense Japan GeoNet Global Navigation Satellite Systems (GNSS) network measured with approximately 1050 stations the coseismic and postseismic surface displacements. We use a novel combination of GNSS, GRACE, and GOCE observations for a distributed fault slip model addressing the issues with gravimetric and geometric change over consistent time windows. Our model integrates the coseismic and postseismic effects as we include GOCE observations averaged over a 2 year interval, but their inclusion reveals the gravity change with unprecedented spatial accuracy. The gravity gradient grid, evaluated at GOCE orbit height of 265 km, has an estimated formal error of 0.20 mE which provides sensitivity to the mainly coseismic and integrated postseismic-induced gravity gradient signal of −1.03 mE. We show that an increased resolution of the gravity change provides valuable information, with GOCE gravity gradient observations sensitive to a more focused slip distribution in contrast to the filtered GRACE equivalent. The 2 year averaging window of the observations makes it important to incorporate estimates of the variance/covariance of unmodeled processes in the inversion. The GNSS and GRACE/GOCE combined model shows a slip pattern with 20 m peak slip at the trench. The total gravity change (≈200 μGal) and the spatial mapping accuracy would have been considerably lower by omitting the GOCE-derived fine-scale gravity field information.

1. Introduction

The 2011 Tohoku-Oki earthquake occurred with an estimated magnitude of 9.0 M_w on 11 March at 05:46 UTC [*U.S. Geological Survey*, 2014] and was the largest megathrust earthquake in Japan that has been recorded with modern spaceborne geodetic techniques.

The dense GeoNet Global Navigation Satellite Systems (GNSS) station network (with approximately 1050 stations located on the mainland of Japan) indicated a maximum coseismic displacement of 5.3 m horizontally and 1.2 m vertically [*Nishimura et al.*, 2011]. In addition, the distinct local change in Earth's gravity field was measured with the spaceborne gravity missions Gravity Recovery and Climate Experiment (GRACE) [*Matsuo and Heki*, 2011; *Han et al.*, 2011] and Gravity Field and Steady-State Ocean Circulation Explorer (GOCE) [*Fuchs et al.*, 2013]. The associated gravity change, derived from GRACE data, is thereby close to the overall mission measurement performance, and therefore, tailored data processing is required to reveal the seismic-induced gravity signatures [*Matsuo and Heki*, 2011; *Han et al.*, 2011].

Distributed slip models, which model the intrinsic movements of plate segments along the Japan trench, are usually derived from GNSS and/or seismic data. Additionally, seafloor GNSS and/or tsunami data have been recently combined with the aforementioned data to enhance the spatial sensitivity of the derived slip distributions [e.g., *Hooper et al.*, 2012; *Bletery et al.*, 2014]. Gravity data are an additional and independent observation type that are increasingly used in estimating point source earthquake models [*Han et al.*, 2011; *Matsuo and Heki*, 2011; *Wang et al.*, 2012; *Cambiotti and Sabadini*, 2013] or distributed slip models [*Cambiotti and Sabadini*, 2012]. Here we introduce novel gravity gradient data and combine them with GNSS observations for distributed slip modeling. Furthermore, we address the combination of observation types with different sensitivities to slip and different spatial resolutions following our previous work in *Fuchs et al.* [2013] and *Fuchs et al.* [2015].

Here we study whether gradients derived from the GOCE mission (2009 to 2013), which enable mapping of gravity details typically at a resolution between 500 and 80 km, can enhance the geophysical modeling in terms of spatial resolution and sensitivity of the fault slip solution in a combination with GRACE and GNSS data.

First, we introduce the GRACE, GOCE, and GNSS data and compute a GRACE and GOCE combined gravity gradient change at mean GOCE orbit height. Second, we show the sensitivity of GRACE and GOCE data in the distributed slip modeling. Finally, we analyze the derived fine-scale gravity gradient change in a joint inversion approach with GNSS deformation data and highlight the modeling implications and geophysical model improvements. The last chapter concludes our work.

2. GRACE and GOCE Satellite Gravity and GNSS Geometric Data

2.1. GRACE Monthly Solutions

The GRACE mission, launched in 2002, measures the Earth's static gravity field and its temporal variations [*Tapley et al.*, 2004]. The GRACE measurement principle is based on a very accurate determination of range differences per time interval (micrometer per second accuracy) between two low Earth orbiting satellites at an orbital height of ≈450 km. The spatial resolution on which the temporal gravity field can be sensed is limited for the Center for Space Research (CSR) series [*Bettadpur and the CSR Level-2 Team*, 2012] up to degree and order 96, corresponding to a ≈200 km half wavelength at Earth's surface. The effective spatial resolution is further limited (typically to ≈350 km) because of the required filtering, which is discussed below. Furthermore, the temporal resolution of the GRACE gravity changes is limited to monthly intervals. This means that a strict separation between coseismic and postseismic gravity changes in the first weeks after the 2011 Tohoku-Oki earthquake is not possible.

It is known that the GRACE mission cannot resolve the very low harmonics and changes in the Earth's flattening (usually described as the spherical harmonic C_{20} coefficient of the gravity field) accurately [*Balmino et al.*, 1999]. Therefore, we replace the C_{20} coefficients of the monthly GRACE CSR series by monthly coefficients from the CSR-SLR series [*Cheng and Ries*, 2014].

One problem of monthly GRACE gravity field products is the inhomogeneous error distribution. Since the GRACE measurement principle is along-track and the ground-track pattern of the GRACE orbital tracks is mainly oriented in north-south direction (due to a polar orbit of the GRACE mission), the measurement system is less sensitive in cross-track (east-west) direction resulting in a less accurate determination of mainly sectorial coefficients of higher order, which corresponds to north-south oriented stripes in the spatial domain.

To show the GRACE-derived gravity change spanning the earthquake and the period afterward, we average a stack of 20 monthly solutions for a 2 year period after the 2011 Tohoku-Oki earthquake and for a period of 1.5 year before (Note that the same periods are used for the GOCE data analysis). We apply 300 km as well as 50 km Gaussian filtering for gravity derived at the reference sphere and the radial gravity gradient derived at 265 km height. Figure 1 shows the derived differences between the 1.5 years before and the 2 years after the earthquake. The 300 km Gaussian smoothing kernel removes part of the coseismic gravity signal but removes almost all sectorial stripes that are dominant when a smoothing kernel of 50 km is applied. The dominance of sectorial stripes in GRACE data after applying the 50 km smoothing kernel is clearly visible in the gravity change (derived at the reference sphere) and in the gravity gradient change derived at GOCE orbit height of 265 km. The sectorial stripes may be suppressed applying a destriping of the global monthly GRACE solutions [*Sweanson and Wahr*, 2006]. Due to the fact that the expected coseismic gravity change resembles a longitudinal bipolar pattern, a destriping filter would thereby remove coseismic gravity change signal. The GRACE-derived gravity gradient change, without applying Gaussian smoothing, shows sectorial stripes which are on the order of several mE (1 mE = 10^{-12} s^{-2}). GOCE gravity gradient measurements (where a single observation, out of the four accurate measured gravity gradients, shows a noise of $\sigma_{V_{zz}} \approx 7$ mE inside the gradiometer measurement bandwidth (MBW)) may thereby act complementary in a long-term average, next to data of the GRACE mission.

2.2. GOCE Data

In contrast to the GRACE mission, the GOCE mission was designed to measure the Earth's fine-scale gravity field, considered as static, with unprecedented accuracy [*European Space Agency*, 1999]. The GOCE mission

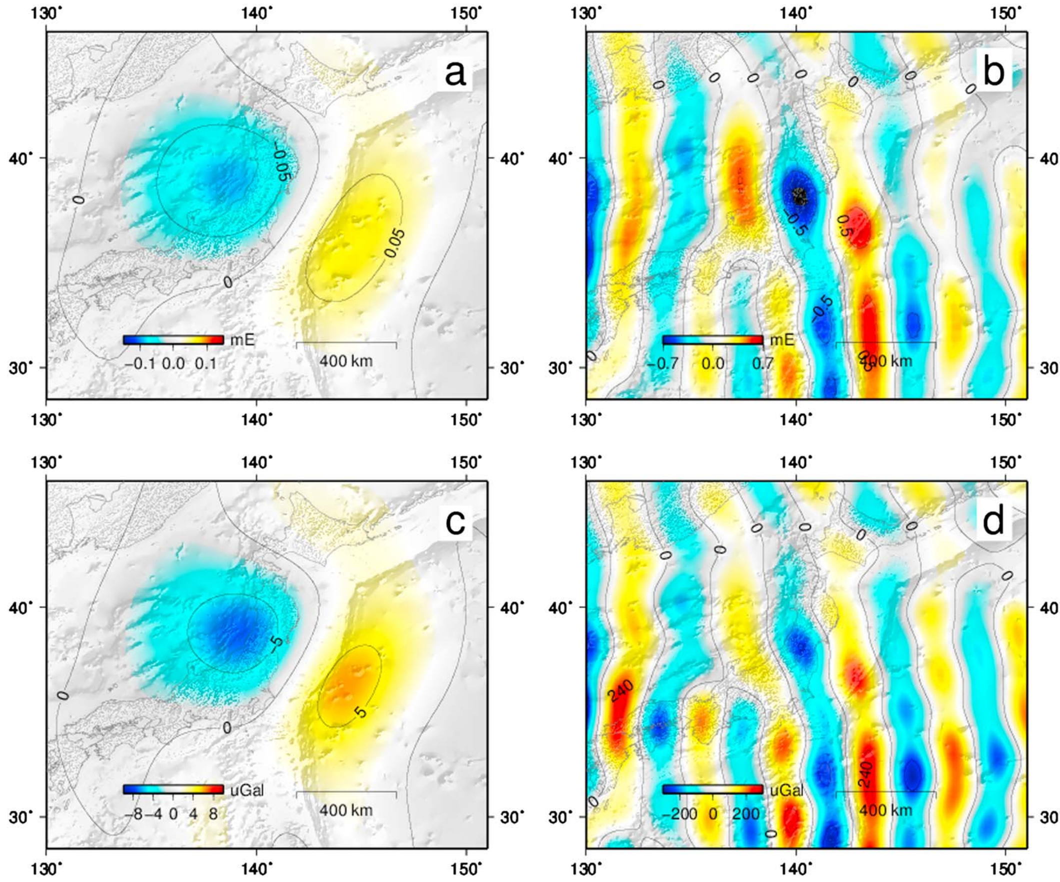

Figure 1. Coseismic gravity and gravity gradient change derived from the GRACE CSR series. (a and c) With 300 km Gaussian filter and (b and d) with 50 km Gaussian filter. Figures 1a and 1b depicted as radial gravity gradients (in mE) at GOCE mean orbit height of 265 km and Figures 1c and 1d depicted as gravity anomalies (in μGal) at the reference sphere.

collected data from November 2009 to October 2013, before the satellite disintegrated on 11 November 2013 into Earth's atmosphere.

The low nominal GOCE orbit height of around 265 km (geocentric distance) and the GOCE onboard gradiometer, which measured the second derivatives of Earth's gravitational potential, are well suited improving global geoid models [*Pail et al.*, 2011; *Bouman and Fuchs*, 2012]. However, by estimating a long-term average, the GOCE gravity gradients are also sensitive to the coseismic gravity change caused by the 2011 Tohoku-Oki earthquake [*Fuchs et al.*, 2013].

We analyzed GOCE data for a 1.5 year period before and a 2 years period after the 2011 Tohoku-Oki earthquake. We stick here to a local gravity field analysis approach, where the four accurately measured GOCE gravity gradients (V_{xx}, V_{yy}, V_{zz}, and V_{xz}) given in the gradiometer reference frame (GRF) are combined. The GRF measured gravity gradient of V_{xx} is pointing approximately in the satellite's flight direction, V_{yy} in cross-track direction, and V_{zz} in radial direction (toward the Earth's center). The combined gravity gradients are a representation of the radial gravity gradient V_{rr} in a local Earth-centered Earth-fixed system [*Bouman et al.*, 2013].

2.3. A Combined GRACE and GOCE-Derived Gravity Gradient Change

The GOCE measured gravity gradients along the orbit suffer from long-periodic noise [*Fuchs and Bouman*, 2011; *Bouman et al.*, 2011], and therefore, data from GOCE alone are not suitable for the study of the coseismic gravity gradient change.

To perform a spectral along-track combination with GRACE, we filter the GOCE gravity gradients to the bandwidth of 10 … 150 mHz using a Butterworth filter of the fourth order, which we apply in forward and reverse direction to preserve phase information. For the lower cutoff frequency we ran simulations from 5 to 12.5 mHz in 2.5 mHz steps and find that 10 mHz optimizes the signal-to-noise ratio for our application. This value is close to the filter cutoff frequency of 8.3 mHz proposed by *Bruinsma et al.* [2013] who combined GRACE and GOCE information globally. As a result, we obtain (for the area of Japan) a flat spectra in the limits of the measurement bandwidth, which can be identified as white Gaussian-distributed noise. The missing long-wavelength part is then replaced by synthetic gravity gradients derived from monthly GRACE CSR solutions. The cut-on frequency of 10 mHz thereby represents approximately spherical harmonic degree 54, which defines the spectral limit where GRACE and GOCE information are weighted equally in the combination. Since the sectorial information of the GRACE monthly solutions is less accurate and the along-track filtered gradients pick up part of the GRACE less accurate sectorial signals (due to the along-track projection of the GRACE information onto the GOCE orbit, see Appendix A), we truncate the series representation at degree 70. This limit defines the transition where GRACE stripes start to dominate in the space domain and where the GOCE-only information tends to be more accurate.

The combination of GOCE and GRACE information improves the sectorial information of the GRACE-only solution but cannot resolve the full sectorial spectra (due to the bandwidth sensitivity of GOCE gradiometry). Therefore, part of the sectorial signal may be omitted because both quantities (GRACE-KBR/GNSS and GOCE gradiometry) are not overall sensitive. For our regional analysis the omitted signals may only have a lower impact on the derived gravity gradient grids because the maximal leakage will occur above degree and order 70 and in addition recovers fast (see Appendix A). In general, GOCE orbit information, derived from the onboard GNSS receiver, could improve the determination of the sectorial coefficients in the gravity field analysis [*Mayer-Guerr et al.*, 2012], but this is not further investigated here. However, in the differences to the background model GOCO03s [*Mayer-Guerr et al.*, 2012] no primarily sectorial anomalies can be observed before and after earthquake occurrence (Figure 3), which means that leakage causes only minor deterioration of the retrieved signals.

2.4. Regional Gravity Gradient Grids

Using the combined gravity gradient data set (section 2.3), we combine the four accurately measured GOCE and GRACE gravity gradient components in a regional least squares estimation. To that aim spherical prisms [*Grombein et al.*, 2011] located at Earth's surface are used to interpolate the measured gravity gradient signals at satellite's mean orbit height in a least squares sense [*Bouman et al.*, 2013]. To compute the gravity gradient grids in an area of interest of 40° by 40°, centered at 37° north and 141° east, we set up a surface grid with nodes of 1° by 1°. This block size is approximately equal to a development of the spherical harmonic series representation to degree and order 180. We studied the truncation of the coseismic modeled gravity signal given in a spherical harmonic series representation and found that the omission of signal above degree and order 180 is below the formal error of the GOCE gravity gradients. Moreover, we choose to combine the gravity gradient information at mean GOCE orbit height because we combine the gradients without any regularization of the solution (unbiased), which would otherwise involve damping of eigenvalues and therefore signal loss. A similar approach has been proposed by *Ebbing et al.* [2013] and *Bouman et al.* [2015] who use gridded gravity gradient products at mean GOCE orbit height for geophysical inversion. Moreover, this approach preserves most of the valuable gradient signal and includes the gravity gradient signals in the modeling considering proper error variances.

Further we study the dealiasing of gravity gradients for the mass effect due to hydrology and Dynamic Ocean Topography (DOT). For the mainland of Japan, hydrological changes derived from the GLDAS model [*Rodell et al.*, 2004] have an equivalent water column at centimeter level (evaluated for monthly intervals at ≈200 km spatial scale), which gives a negligible gravity gradient signal of V_{rr} at GOCE orbit height of 0.01 mE (the signal is well below the estimated GOCE gradient formal error shown in Appendix B). In contrast, the DOT of the oceanic current Kuroshio in the vicinity of Japan shows a standard deviation in sea level height of 0.6 m derived from multialtimetry satellite missions [*Schwatke et al.*, 2010]. We compute the V_{rr} correction due to a mass change originated by DOT (resolution of 0.25°), which is shown in Figure 2. The gradient signal exceeds 0.12 mE at GOCE orbit height, which is close to the accuracy range of the GOCE-derived formal errors of the mean fields (Appendix B). Because no mass changes due to DOT are considered in GOCE gravity gradient products, we apply a temporal DOT correction to the GOCE gravity gradients, which is shown for the mean fields (Figure 3c).

For our study no appropriate gravity reference model is available, because the focus of the GOCE mission is the static gravity field where no temporal gravity field solutions are available. We therefore computed as reference

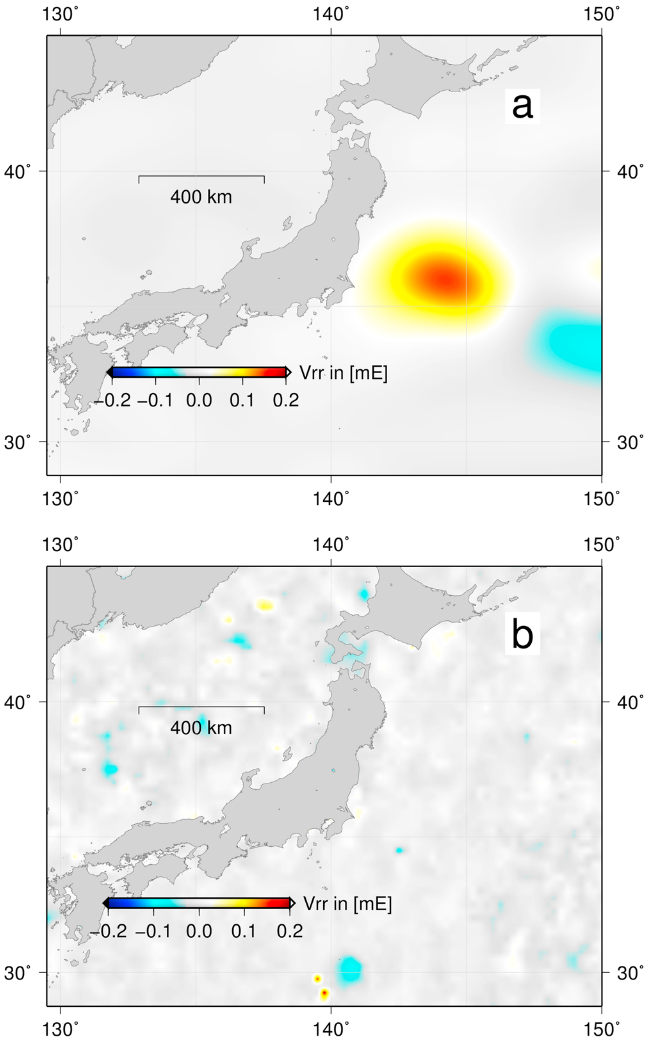

Figure 2. (a) DOT mass-induced signal for T_{rr} at mean GOCE orbit height of 265 km derived from altimetry. (b) Nontidal correction for GOCE gravity gradients. Both plots are derived for identical periods.

a static solution based on 1.5 year data before earthquake occurrence (Figure 3a). In addition, we compute a 2 year averaged solution (Figure 3b) after earthquake occurrence. Figure 3 shows the derived gravity gradient differences at GOCE mean orbit height relative to the global gravity field model GOCO03s [*Mayer-Guerr et al.*, 2012]. Finally, we difference both periods and subtract the DOT correction to obtain a co- and integrated postseismic gravity gradient change (Figure 3c). One major benefit of the combined GOCE-derived gravity gradient change is that the GOCE information shows an isotropic error pattern in contrast to GRACE-only fields that contain strong longitudinal stripes (Figure 1). Note that no Gaussian filtering has been applied to the GOCE solution shown in Figure 3.

Evaluating the pure signal content of GRACE in the combined GRACE and GOCE gravity gradients (GRACE and GOCE content have been evaluated separately for the grid computation), it can be shown that the introduced signal content is less than < 0.3 mE of the total 1.03 mE maximum signal, which highlights the substantial GOCE fine-scale gravity field contribution (Appendix C). Applying error propagation of both the GRACE monthly fields and the GOCE-derived gravity gradients amounts to a formal error of the derived gravity grids of $\sigma_{V_{rr}} = 0.20$ mE (Appendix B). This value is in agreement with the standard deviation computed for the grids in areas unaffected from the coseismic change, which amounts to a standard deviation of $\sigma_{V_{rr}} = 0.21$ mE.

2.5. GNSS Deformation Data

We use GNSS displacements computed by the Advanced Rapid Imaging and Analysis (ARIA) team at Jet Propulsion Laboratory and Caltech, where the GeoNet RINEX data have been provided to Caltech by the

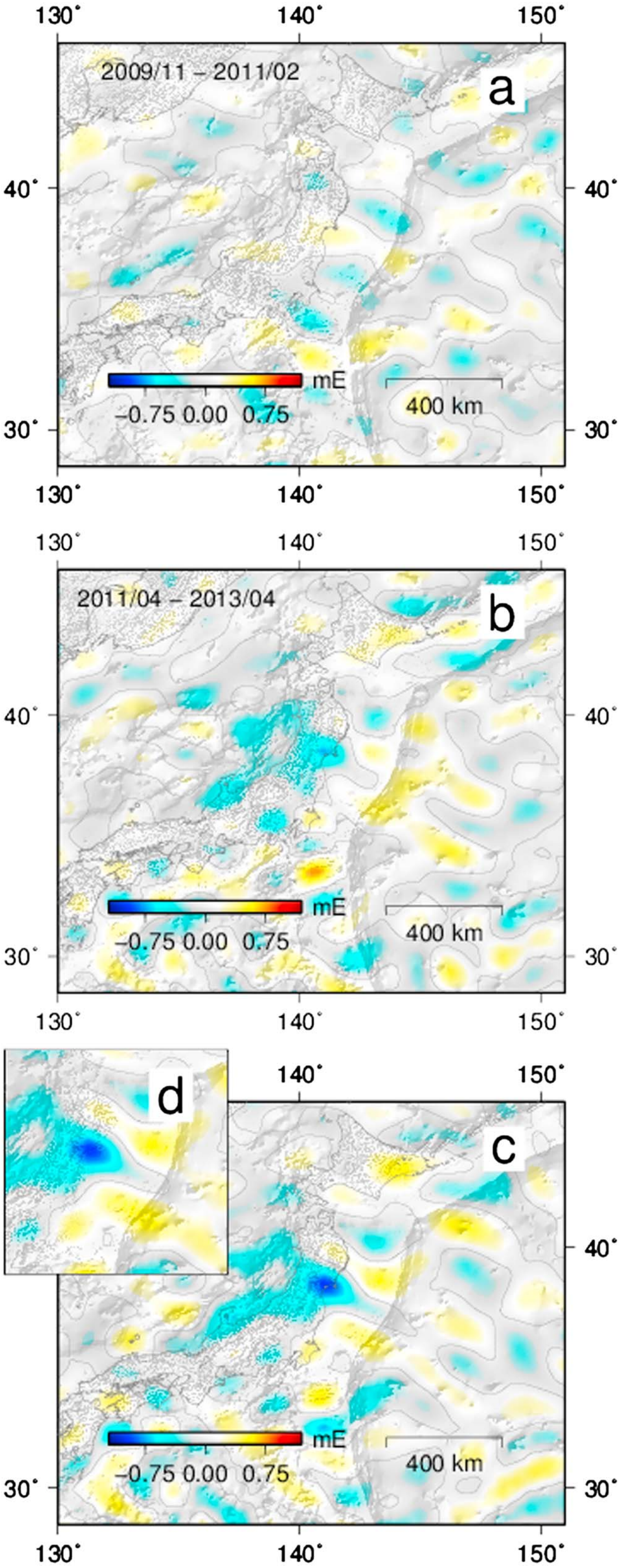

Figure 3. Coseismic V_{rr} gravity change (in mE) derived from all four combined GOCE gravity gradient components. (a) Average of 1.5 years preseismic period, (b) average of 2 year postseismic period, and (c) difference between Figures 3b and 3a applying the DOT correction. (d) The uncorrected difference. Figure 3c is the input data for the distributed slip modeling and applied in the residual plot to the model of Figure 8d.

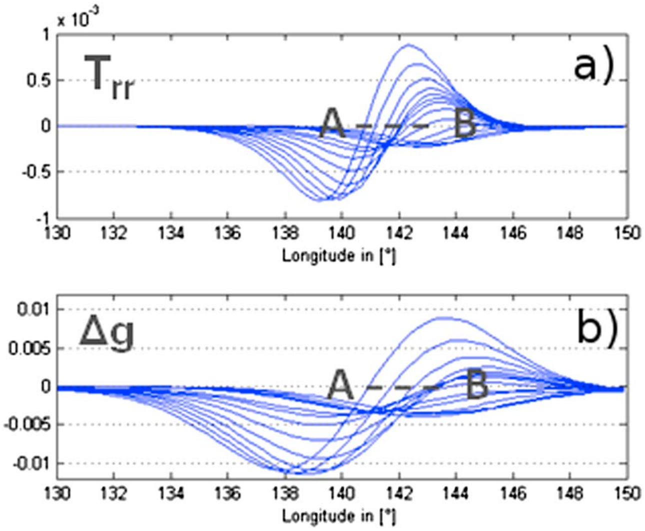

Figure 4. Green's function cross section for unitary dip slip of the distributed slip patches along the profile A-B. (a) GOCE radial gravity gradient T_{rr} in mE at 265 km orbit height, (b) GRACE Δg in μGal at reference sphere. Both functionals show increased amplitude values toward A, which corresponds to deep slip patches.

Geospatial Information Authority (GSI) Japan. Daily GNSS positions have been processed using Jet Propulsion Laboratory's GIPSY/OASIS-II software, applying a single station bias-fixing point positioning strategy [*Zumberge et al.*, 1997; *Bertiger et al.*, 2010].

From the daily GNSS solutions we estimate an annual and semiannual sinusoidal signal and remove this signal from the up-component, based on a 2 years preseismic analysis interval. Moreover, mean velocities of the station positions have been estimated according to IGS08 [*Rebischung et al.*, 2012] and subtracted from the station positions. Stations that show anomalous behavior, e.g., due to jumps and outliers in the data have been discarded. We average the postprocessed GNSS displacements using the same averaging intervals as used for the GRACE/GOCE data: 1.5 years for the preearthquake period and 2 years after the main seismic event. In total 850 stations with three-dimensional position information have been included in the inverse modeling. We derive the variance information, for each individual station position, by evaluating the variance of the residuals between the data and a linear model for (1) a 1.5 year preearthquake quiescence period and (2) a 2 year postseismic period. Both values have been further applied in the inverse modeling (section 4).

3. GRACE and GOCE Sensitivity in a Distributed Slip Model

Summarizing, three different data sets were used for this study: (1) Monthly GRACE solutions, from the CSR-R05 series (where C_{20} has been replaced by values derived from SLR) (section 2.1); (2) GOCE calibrated and corrected gravity gradient observations evaluated at GOCE orbit height of 265 km above the reference sphere (6,378,137 m) (section 2.2); and (3) daily GNSS positions measured by the GeoNet station network located on the mainland of Japan, which we have subsequently postprocessed to remove nontectonic signals (section 2.5).

All data sets may show different sensitivities to changes in the distribution of slip in strike and dip direction along the Japan fault interface (Note that a detailed distributed fault slip model geometry is given in section 4). The GNSS sensitivity has been analyzed in various studies, e.g., *Hoechner* [2010] or *Feng and Jónsson* [2012]. We focus on the difference between the GRACE and the GOCE mission in evaluating the mission-related gravity functionals for the 2011 Tohoku-Oki earthquake.

We computed gravity Green's functions for unit slip (both for pure dip slip and pure strike slip) for patches on a fault plane using the semianalytical normal mode model [*Sabadini and Vermeersen*, 2014] up to degree and order 450, with a cosine taper applied from degree 300 on. The modeled gravity changes due to slip include the effect of seawater displacements [*Broerse et al.*, 2011]. When modeling the bathymetry changes that drive these seawater displacements, we include the effect of horizontal displacements of the steep seafloor [*Satake et al.*, 1996; *Hooper et al.*, 2012; *Bletery et al.*, 2015] on gravity changes [*Broerse et al.*, 2014]. Our method includes realistic coast lines and is gravitationally self-consistent.

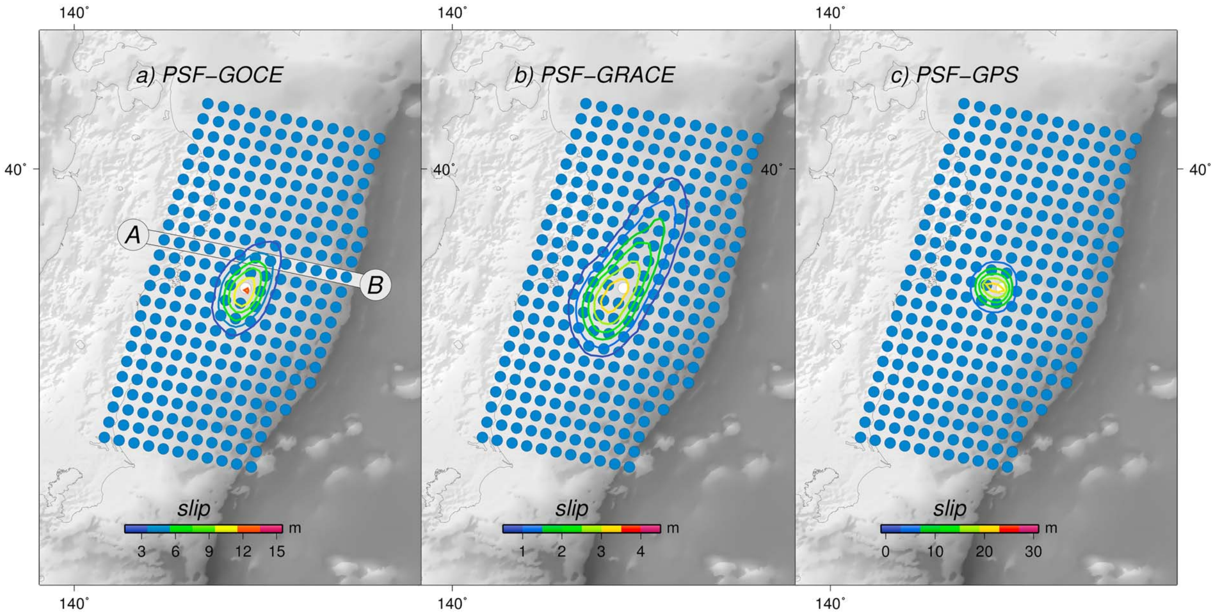

Figure 5. Point spread functions (PSF) derived for (a) the GOCE mission applying T_{rr}, (b) the GRACE mission applying Δg, and (c) GNSS data for the central slip patch indicated in white. GRACE shows a coarse distributed PSF where the GOCE PSF is more focused especially in along-strike direction. GNSS shows here the most focused slip reconstruction.

Figure 4 shows the profile of the computed Green's functions for unit dip slip along the slip patch row A-B of the distributed model patches depicted in Figure 5. The GRACE gravity Green's functions for Δg (gravity change) follow a broad distribution compared with the radial gravity gradient changes ΔT_{rr} at GOCE mean orbit height, which are more focused. Due to increasing density with depth (see Appendix D—stratification model), the gravity change for unit slip also increases for deeper slip patches, which indicates that both missions (GOCE and GRACE) are mostly sensitive to deep slip. Moreover, Figure 4 indicates that GRACE and GOCE might be less sensitive to slip close to the trench, since shallow slip has a relatively small effect on the broadscale gravity changes.

We perform a simulation study based on the Green's functions of the distributed fault slip model. Using synthetic gravity changes due to slip on a single finite fault patch, we invert for slip where the spatial mapping of inverted slip results in a corresponding point spread function (PSF). Since the synthetic input quantity can be compared with the estimated slip, the PSF is a measure of how well slip, derived from a certain slip patch, is recoverable. Figure 5 shows the PSF for (a) GOCE, (b) GRACE, and (c) GNSS data, applying 100 m of dip slip to the test patch (indicated in white). All three solutions have been computed with identical inversion setups with the prior probability for the rake angle set to be constant between $\pm 35°$ of the convergence direction and zero otherwise. Figure 5 shows that gravity gradients of the GOCE mission are spatially more sensitive to slip compared to the filtered GRACE-only solution. The synthetic gravity gradients recover a more focused slip distribution and estimate maximum amplitudes closer to the modeled slip (approximately three times more focused). The increased spatial sensitivity of GOCE data improves especially the along-strike sensitivity. We perform a similar test for GNSS data only (Figure 5c) and find that GNSS has higher resolving power for slip than spaceborne gravimetric techniques: the GNSS PSF is more focused and resolves 60% higher maximum slip than the gravity gradient PSF. However, even GNSS has spatial limitations due to regularization applied.

Besides the PSF test we also perform a checkerboard test, shown in Figure 6. The result for the GNSS-only solution shows that terrestrial GNSS is restricted in its sensitivity to the half of the fault plane closest to the network. This finding is in agreement with, e.g., *Diao et al.* [2012]. Including synthetic gravity gradient data, extends the sensitivity right up to the trench and improves the overall resolving power over the whole fault plane. The integrated inverse modeling, which includes gravimetric and geometric observations, may therefore benefit from a combination of geometric and gravimetric observation types, compared to a solution merely derived from GNSS data. We did not use GRACE data for a checkerboard test because from Figure 5b it can be seen that the checkerboard resolution is not compatible with the spatial extent of the GRACE-PSF.

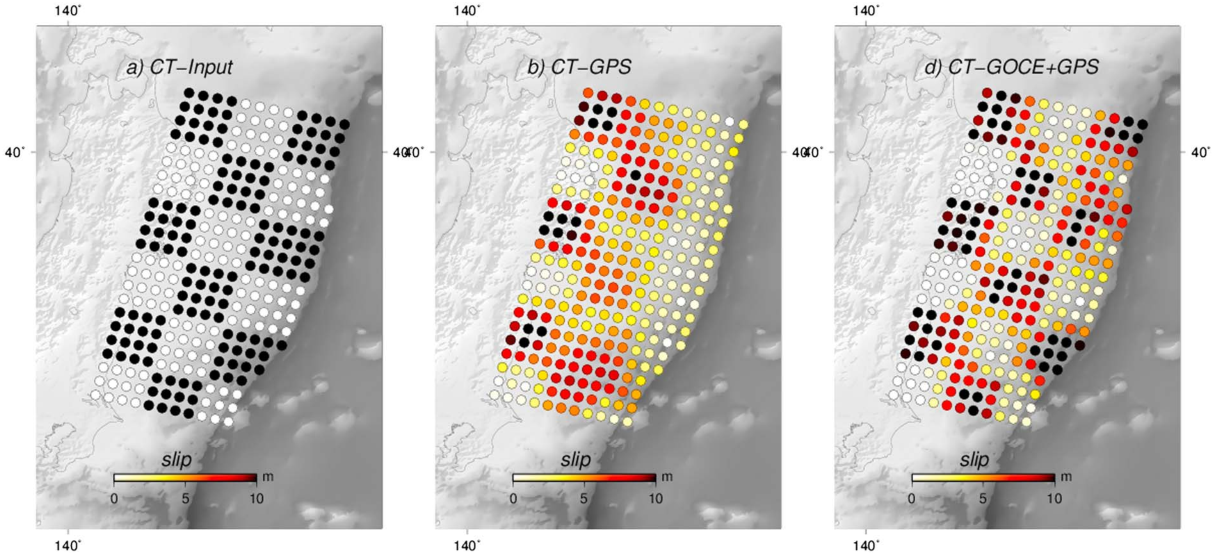

Figure 6. Checkerboard test performed over the modeled fault plane. (a) The input mode, (b) the reconstruction of the fault plane using GNSS only, and (c) using the combined inversion of GNSS and GOCE data. Both setups use a rake angle limit of ±35°which differs to the GNSS-only inversion performed in Appendix F.

4. The Joint Inversion of GNSS and Gravity Gradient Data

For the combination of gravitational and geometric observation types, a preexisting joint inversion approach based on Bayes theorem for conditional probability has been used [*Hooper et al.*, 2012], where gravitational functionals are implemented with Green's functions and appropriate variance weights according to *Fuchs et al.* [2015]. The model applies a Markov chain Monte Carlo algorithm [*Mosegaard and Tarantola*, 1995; *Hooper et al.*, 2011] to find the posterior slip probability distribution for each slip patch, respectively, applying the Laplacian of the slip distribution as smoothing constraint. The posterior probability distribution for the model parameters is given by

$$p(\mathbf{s},\alpha^2|\mathbf{d}) = p(\mathbf{s})\cdot K\cdot[\alpha^2]^{-M/2}e^{[-\frac{1}{2}(\mathbf{d}-\mathbf{Gs})^T(\mathbf{\Sigma_d}+\mathbf{\Sigma_m})^{-1}(\mathbf{d}-\mathbf{Gs})-\frac{1}{2}(\mathbf{Ls})^T(\mathbf{Ls})]} \tag{1}$$

where $p(\mathbf{s},\alpha^2|\mathbf{d})$ represents the posterior probability distribution, $p(\mathbf{s})$ is the a priori probability distribution, K is a scaling constant, α^2 is the regularization parameter, $\mathbf{G}$ is a matrix containing the Green's functions, $\mathbf{s}$ is a vector containing the slip and rake model parameters for each fault patch, $\mathbf{L}$ is the Laplacian operator, $\mathbf{d}$ is a vector containing the observations, $\mathbf{\Sigma_d}$ is the data variance-covariance matrix, $\mathbf{\Sigma_m}$ is the model variance-covariance matrix, and M is the number of model parameters.

The fault model includes 283 fault patches with a fixed strike for all patches of 194.43°. The single patch size for a subfault element is 25 km along strike and 20 km downdip, resulting in a model area of approximately 260 × 575 km. We use here the fault plane reconstruction based on *Gou et al.* [2006] with two consecutive planes where a dip angle of 5° is used from the trench up to 80 km off the trench and a dip angle of 15° beyond. We do not enforce Laplacian smoothness at the fault edges, which we achieve by applying cubic extrapolation at the edges of the fault, rather than assuming zero slip there. This can be seen in the provided checkerboard tests (Figure 6) where slip extends to the model boundaries.

We derive two different distributed slip models (see Figures 7a and 7b). Setup (1) uses GNSS data error variance information derived from a 1.5 year preearthquake quiescence period (section 2.5) and variance information of the gravity gradient grids (Table B1) where data covariance information for both techniques and model errors have been neglected. Setup (2) includes estimates of data error and model error variance and covariance. The GNSS data variance information was derived from a 2 year postseismic period, which results in a more conservative error estimate as compared to setup (1) (section 2.5). The gravity gradient grid data covariance has been estimated in the area of the Taklamakan dessert (almost the same latitude as Japan), because here it is assumed that no temporal gravity changes take place. The covariance has been derived from a 1 and a 2 year averaging period where the latter is used as reference to compute a residual gradient change signal and to derive the covariance weight matrix.

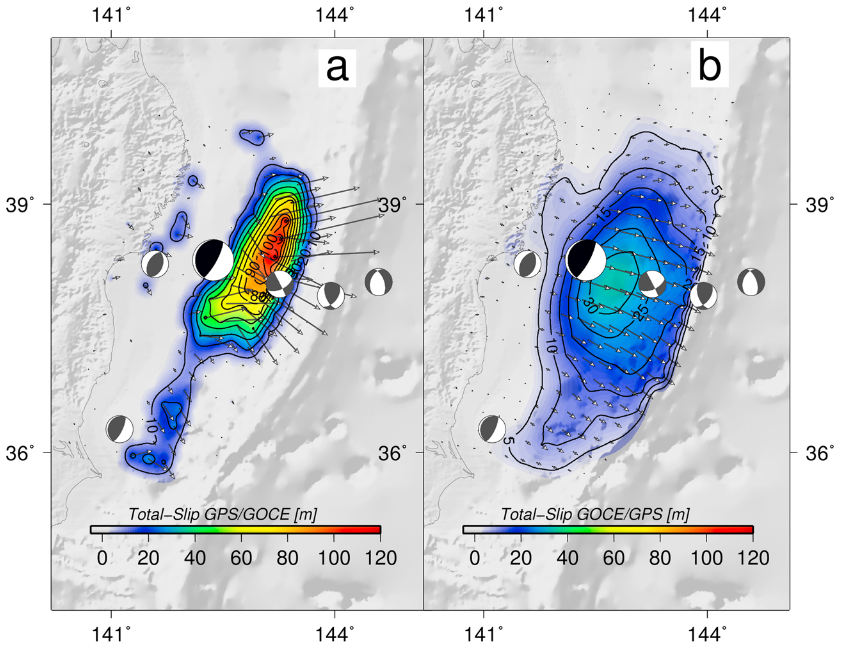

Figure 7. Slip distribution derived from the combination of GNSS and GRACE/GOCE data where (a) setup (1) and (b) setup (2) is applied. For both solutions the rake angle can vary between ±35°. The arrows are slip vectors derived from the model prediction. The maximum slip for each patch has been indicated by the given color scheme. Contour lines have been introduced for Figure 7a in steps of 10 and for Figure 7b in steps of 5 m. The beach balls indicate aftershocks for the 2 years postseismic period for magnitude $\geq 7.0\ M_w$. The slip solutions are the mean of the full posterior probability distribution where setup (1) considers data errors only where setup (2) also considers model errors introduced by postseismic processes not related to afterslip.

To estimate the model error, we assume that this is dominated by postseismic processes other than afterslip, chiefly viscoelastic relaxation. We use the estimate of the viscoelastic mantle relaxation contribution to the total postseismic moment from *Diao et al.* [2014] and extrapolate their 1.5 years estimate to a 2 year postseismic period. This leads to an estimate that around 10% of the 2 year postseismic moment is not afterslip related. Furthermore, we assume that the seismic moment scales linearly with the derived GNSS postseismic deformation (Figure 9) and the postseismic gravity gradient change. We then estimate the covariance between each pair of observations as the product of 10% of the postseismic signal estimated for each of the observations.

To include the model errors in the inversion, the inversion scheme is updated according to *Tarantola* [2005], where the variance-covariance matrix is given by the sum of the data and model error variance-covariance matrices (see equation (1)). The nondiagonal terms of the data error variance-covariance matrix are small for GNSS compared to the corresponding model error terms, and we neglect them in contrast to the gravity gradient data. The diagonal of the weight matrix for setups (1) and (2) approximately differs by a relative factor of 10, which indicates that an adequate postseismic error assessment is essential for the combined distributed fault slip modeling of gravimetric and geometric techniques for a 2 year averaging period. Including the postseismic model errors in the inversion results in a relative downweighting of GNSS data in the combined inversion, because the signal-to-noise ratio of gravity gradient data is much smaller as compared to the signal-to-noise ratio for the derived GNSS displacement data.

Figure 7a shows the derived distributed fault slip model for a combination of GNSS and GRACE/GOCE data applying variance weights following setup (1). Figure 7b shows a distributed fault slip model for a combination of GNSS and GRACE/GOCE data where GNSS data have been weighted according to setup (2). Considering covariance in the inversion scheme, in setup (2), causes GRACE/GOCE data to gain significant impact on the combined solution.

We also computed a GNSS-only solution (Appendix F) with prior probability for rake angle between ±20° as opposed to ±35° for setups (1) and (2). For all three models we find similar values for the maximum a posteriori estimate of moment magnitude: (a) 9.12 M_w (setup (1)), (b) 9.11 M_w (setup (2)), and (c) 9.13 M_w (GNSS-only solution).

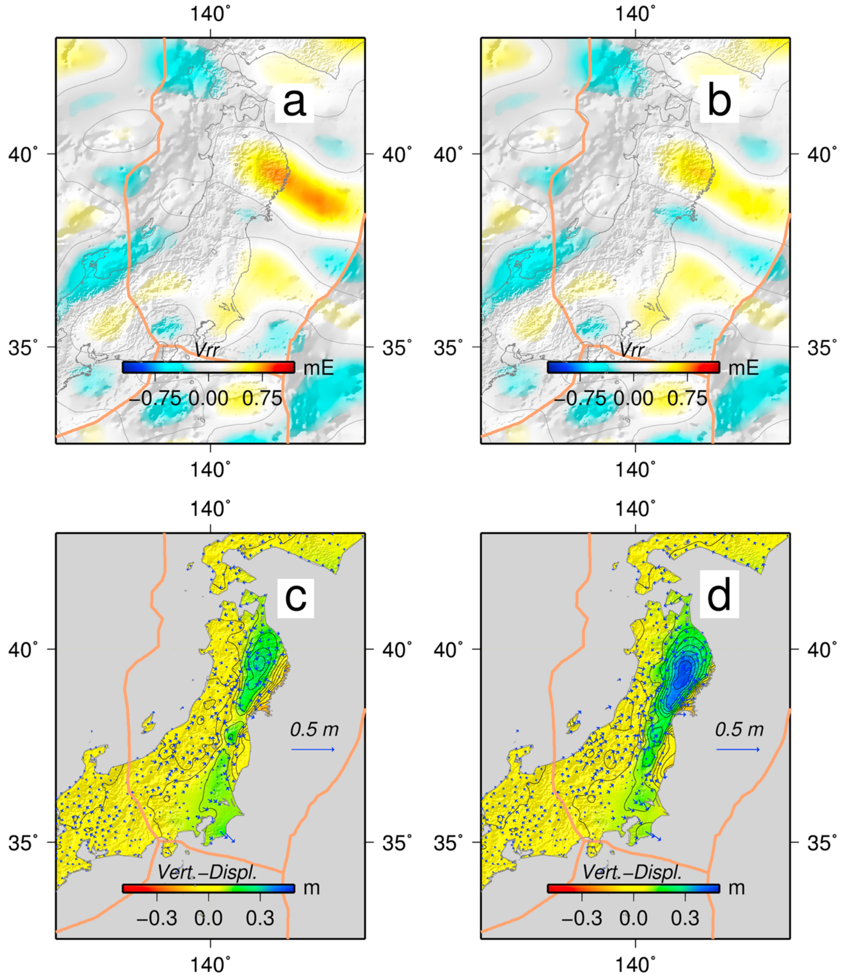

Figure 8. (a and b) The model residuals for the radial gravity gradient data (shown in Figure 3c) for V_{rr} at 265 km altitude. (c and d) The model residuals for the 850 selected GNSS stations. Figures 8a and 8c are computed applying setup (1), and Figures 8b and 8d are computed applying setup (2). All residuals are defined as observed minus modeled signals.

Using the combined GRACE, GOCE, and GNSS slip distribution of Figure 7b, we compute the total gravity field change using gravity Green's functions at ground (derived up to degree and order 450 with a cosine taper starting at degree 300 applied). The total gravity field change amounts at the reference sphere to -349 μGal and $+276$ μGal, respectively, which equals a geoid change up to $\approx$ 1.5 cm (Appendix G).

5. Discussion

As shown in Figure 7, the effect of a larger weight of the gravity gradient data in the inversion is a smoother slip distribution, with a lower peak amplitude and slip more broadly distributed along strike and dip. Moreover, setup (1) results in a rake distribution with high spatial variability, whereas the higher weight of the gravity data in setup (2) forces the rake angle to be largely parallel to the convergence direction. Evaluating the model fit shown in Figure 8, we find that the horizontal components of the GNSS measurements fit the derived models in general well ($\sigma_{\mathrm{GNSS}} < 4$ cm with all residuals < 19 cm). However, for the vertical GNSS component there are significant model residuals. For the combination based on setup (2) the residual pattern of the vertical GNSS component shows up significantly at the central area and toward north of Japan (Figure 8d).

We analyze the postseismic GNSS displacements during the first 2 years after the 2011 Tohoku-Oki earthquake (Figure 9) where we use the coseismic change from *Hooper et al.* [2011] and subtract the station position estimates from the 2 year integrated solution. Figure 9c shows a displacement, which is spatially in agreement with *Ozawa et al.* [2012] but amplifies the derived trend of the first 20 days of postseismic displacement. The displacement of Figure 9c shows a clear uplift pattern at coastal areas and in the area where also the gravity

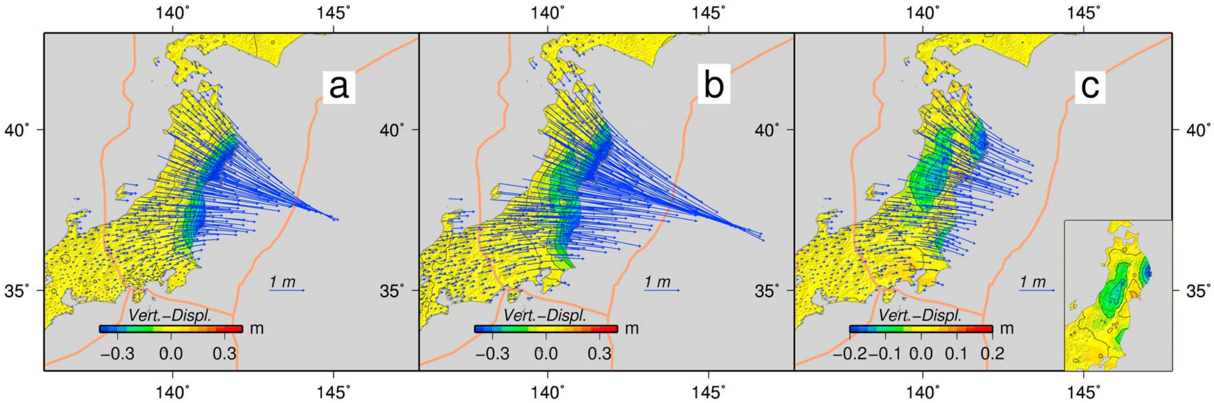

Figure 9. (a) The derived coseismic displacement. (b) The 2 year averaged displacement. (c) The difference between coseismic and the 2 years averaged postseismic displacement.

gradient change is largest. The residual patterns of Figures 8c and 8d are similar to the model residuals of Figure 9c and therefore indicate that the postseismic uplift in this area may map to GNSS-derived solutions [see also *Ozawa et al.*, 2012]. Moreover, the large residuals also show up for a solution derived only from GNSS data (Appendix F). This indicates that model errors must be accounted for, which has been implemented in the GNSS/gravity inversion of setup (2).

Computing a GNSS-only solution with a constraint on the rake angle of ±20° (Appendix F) shows a more homogenous slip pattern, which is similar to the combined slip derived from setup (2) (Figure 7b). The GNSS residuals (Appendix F) increase in the same areas as for the GRACE/GOCE and GNSS combined solution (Figures 8c and 8d). Limiting the rake angle further to ±10°(not shown here) increases the residuals of the GNSS measurements to the same level as for the GRACE/GOCE and GNSS combined solution derived for setup (2) (Figure 8d).

The gravity gradient residuals derived with setup (1) (Figure 8a) show a positive gravity gradient residual pattern to the north. Moreover, the positive pattern of Figure 8a originates from the strong strike-slip component of the diffuse rake angle pattern that shows increased gravity gradient signal outside the focal area. Applying proper variance/covariance information in the inversion does lower the gravity gradient residuals significantly. Evaluating the solution merely derived from GNSS data (Appendix F) shows a negative gravity gradient peak of Figure F1b which can be attributed to the larger estimated total slip (Figure F1a) taking place at the focal area. Therefore, gravity gradient data provide, in addition to the constraint on the rake angle, valuable information on the total integrated slip (potency).

Our combined slip model predicts less slip than needed for the observed near-trench horizontal displacement of about 50 m by *Fujiwara et al.* [2011]. The maximum slip of our combined model (setup (2)) is also less than the 60 m as inferred by *Bletery et al.* [2014] and the 73–81 m as inferred by *Hooper et al.* [2012]. Maximum slip is, however, dependent on the resolution provided by the data, and we did not include tsunami data as these studies did (Figure 4).

Due to the fact that the solution spans 2 years, the results of the derived slip distributions should be interpreted with care because averaging over a 2 year period integrates both coseismic and postseismic changes. Our combined solution of Figure 7b shows a more extended pattern (north-south) and includes additional deep slip in contrast to coseismic models [e.g., *Hooper et al.*, 2012; *Bletery et al.*, 2014]. Other postseismic studies such as *Diao et al.* [2014], *Fuchs et al.* [2015], and *Yamagiwa et al.* [2015] found a deep-slip pattern for postseismic periods, mostly taking place in regions not affected by the coseismic rupture of the 2011 Tohoku-Oki earthquake, which may be connected to areas of coseismically increased Coulomb failure stress [*Diao et al.*, 2014]. In addition, any postseismic deformation and gravity changes due to mantle relaxation [*Sun et al.*, 2014; *Han et al.*, 2014] are wrongly interpreted in our model as slip. However, *Yamagiwa et al.* [2015] presented a model in which the viscoelastic contribution is on the order of decimeters and might account for less than 10% of the total displacement signal. Likewise, *Diao et al.* [2014] found that viscoelastic relaxation within the 1.5 years postseismic period plays only a secondary role on the assumption of a $2 \cdot 10^{19}$ Pa s Maxwell viscosity and neglecting transient viscoelastic relaxation. We estimated from the 2 years postseismic gravity gradient change a linear trend (Appendix E) and found no significant rate (Note that the uncertainty of the estimated trend is large ≈0.41 mE/a). Viscoelastic mantle relaxation at larger scales has a small net amplitude [*Han et al.*, 2014] for which GOCE data may not be appropriate for analysis. For example, analyzing a 1 year postseismic period following the Sumatra-Andaman earthquake states a gravity change, derived from GRACE data (up to degree and order 40), to be in the order of 3.5 μGal [*Broerse et al.*, 2015]. This would correspond to a gravity gradient signal at GOCE orbit height of 0.02 mE.

6. Conclusions

We show for the first time the joint inversion of GRACE and GOCE combined gravity gradient data with GNSS displacement data integrated in a Bayesian inversion model for a 2 year averaging period. The derived fine-scale gravity gradient information of the GOCE mission, mapped with unprecedented spatial accuracy, offers a benefit in the inversion of fault slip modeling, because gravity gradient data are an independent and complementary observable next to displacement data derived from GNSS. The derived gravity gradient changes provide measurements over land and oceanic terrain but also involve different sensitivities compared to fault slip solutions merely computed from GNSS data.

We find a good agreement between our combined model and the horizontal GNSS displacements (RMS of the residuals $\sigma_{\text{GNSS}} \leq 4$ cm) and the gravity gradients (absolute signal residuals ≤ 0.2 mE). The GNSS local up-component shows less agreement when gravity gradient information is significantly integrated in the inversion. This may be due to a mismodeling of gravity or surface deformation but is more likely due to a postseismic uplift pattern in the north of Japan as measured by GNSS data.

Zhou et al. [2014] and *Loveless and Meade* [2011] have shown that constraining a priori the rake angle can lead to significant differences in derived slip models. Including gravity gradient data in a combined inversion significantly improves the constraint of the rake angle without having to arbitrarily impose prior constraints. In addition, gravity data provide sensitivity on the total slip, which results from the integral slip over the area. The derived gravity Green's functions indicate only a moderate sensitivity of GOCE gravity gradient data close to the trench.

Because of the necessity to average the data over 2 years, significant nonmodeled processes are included in the observations. Including model error variance-covariance then becomes an important consideration and leads to more reliable results.

Appendix A: Geometric Along-Track Projection

Figure A1 depicts a schematic of along-track projection of GRACE and GOCE information in the space and spectral domain.

Appendix B: Estimated Formal Errors of the Gravity Gradient Grids

The variances of the preseismic and postseismic periods have been derived in four intervals using error propagation of the observations (see Table B1). Between periods (1) and (2) a major difference in the measurement quality due to an onboard switch of the GOCE measurement system from CPU-A to the CPU-B side affects the

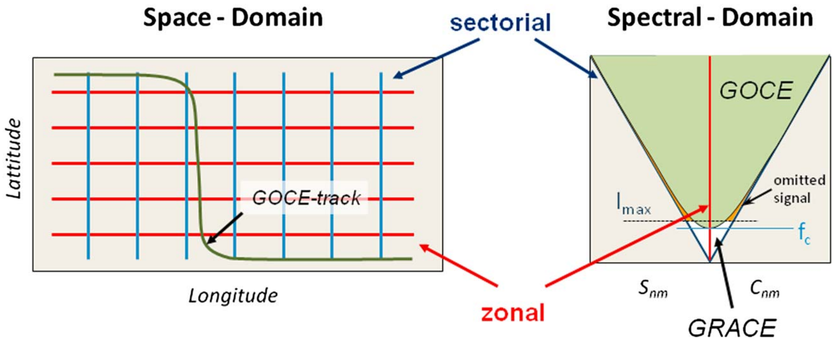

Figure A1. Schematic of along-track projection of GRACE and GOCE information depicted in the space and spectral domain.

Table B1. Formal Errors Estimated From the Combination of the Gravity Gradient Measurements Given in the GRF Derived at the Mean Orbit Height of 265 km in the Earth-Centered Earth-Fixed System[a]

Interval	1	2	3	4
Start Date	Nov 2009	Mar 2010	Apr 2011	Apr 2012
End Date	Mar 2010	Feb 2011	Apr 2012	Apr 2013
σ of V_{rr}	0.30 mE	0.20 mE	0.19 mE	0.15 mE
Average of (1 + 2) and (3 + 4)	0.17 mE		0.12 mE	
Difference of average intervals	0.20 mE			
σ of $\partial V_{rr}/\partial t$			$0.68\ \frac{\text{mE}}{a}$	$0.52\ \frac{\text{mE}}{a}$
Average			$0.41\ \frac{\text{mE}}{a}$	

[a] This formal errors represent the sum of the GOCE-derived gravity gradient error and the error propagated from monthly solutions of the GFZ series. Note that the CSR series does not provide an error estimate for their solution.

derived variances. Due to the fact that period (1) is computed from approximately half a year data, the periods (1) and (2) have been weighted one third to two thirds in the average. Periods (2) to (4) have been weighted equally since the variances are almost in the same range.

Appendix C: Signal Contribution of GRACE and GOCE Gravity Data

Figure C1 shows a single contribution for the combined gravity gradient change derived from (a) GRACE, (b) uncorrected GOCE, and (c) GOCE with DOT correction.

Appendix D: Stratification Model

The derived gravity Green's functions indicate only a moderate sensitivity of GOCE gravity gradient data close to the trench. Because of the necessity to average the data over 2 years, significant nonmodeled processes are included in the observations (see Table D1). Including model error variance-covariance then becomes an important consideration and leads to more reliable results.

Appendix E: Gravity Gradient Linear Trend Evaluated for a Two Year Period

Postseismic gravity trend is less accurately determined due to lower track coverage and the increasing orbit height of the GOCE satellite (see Figure E1). GOCE gravity gradients seem insensitive to postseismic trends.

Appendix F: Modeled Geoid Heights

Figure F1 shows geoid heights computed from the GNSS and GRACE/GOCE.

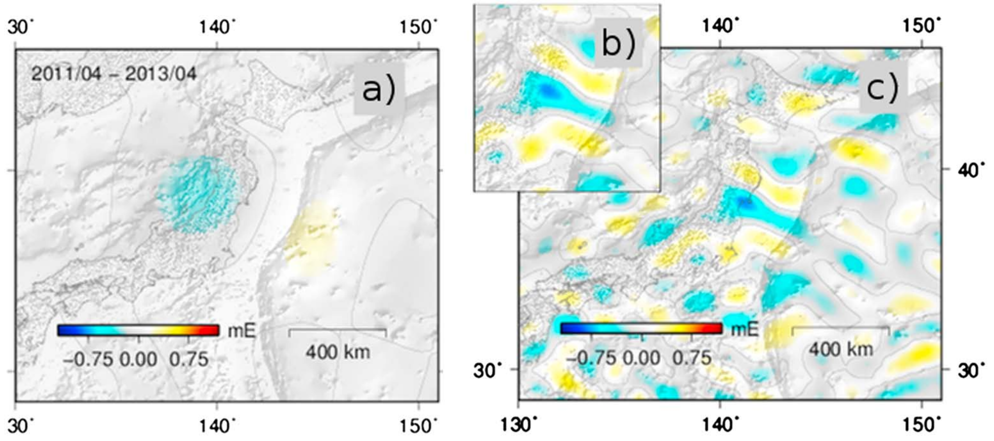

Figure C1. Single contribution for the combined gravity gradient change derived from (a) GRACE, (b) uncorrected GOCE, and (c) GOCE with DOT correction.

Table D1. Elastic Earth Model Parameters

Layer	r (km)	ρ (kg/m^3)	μ (N/m^2)	λ (N/m^2)
1	6371	2,732.00	0.341×10^{11}	0.395×10^{11}
2	6347	3,380.00	0.677×10^{11}	0.858×10^{11}
3	6331	3,371.00	0.670×10^{11}	0.840×10^{11}
4	6151	3,698.00	0.940×10^{11}	1.420×10^{11}
5	5701	4,878.00	2.190×10^{11}	3.130×10^{11}
6	3480	10,932.00	0.000×10^{11}	0.000×10^{11}

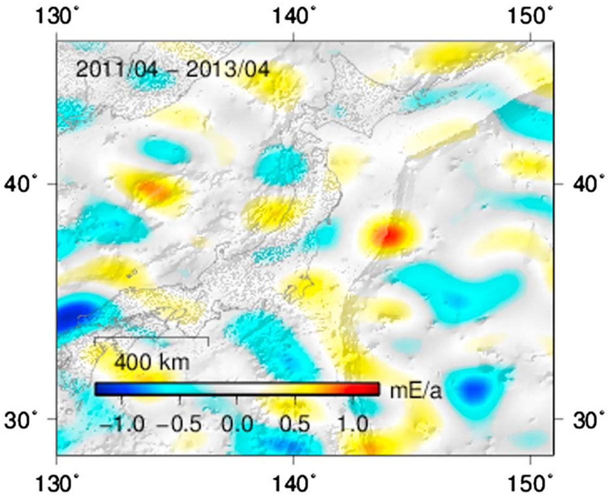

Figure E1. Postseismic gravity gradient trend evaluated for a 2 years period. Note that toward the south, the trend is less accurately determined due to lower track coverage and the increasing orbit height of the GOCE satellite. GOCE gravity gradients seem insensitive to postseismic trends at the focal area due to a comparable large formal error.

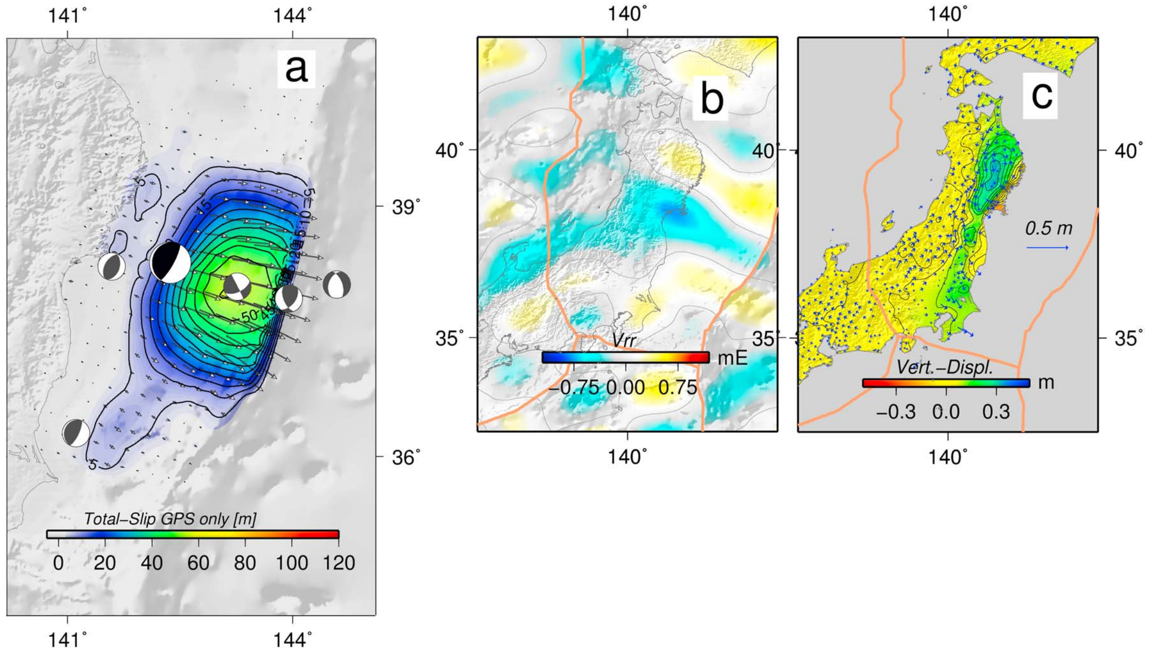

Figure F1. Geoid heights computed from the GNSS and GRACE/GOCE combined slip distribution up to degree and order 450 with a tapered cosine filter applied above degree and order 300.

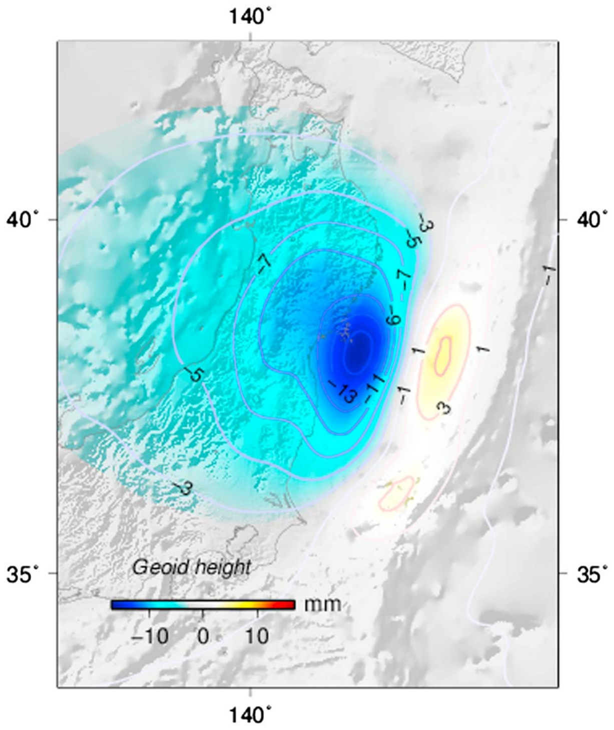

Figure G1. GNSS-only solution derived with a rake angle constraint of ±20°. (a) The derived slip distribution, (b) the gravity gradient residuals at 265 km altitude, and (c) GNSS station residuals.

Appendix G: GNSS-Only Model and Residuals

Figure G1 depicts the GNSS-only solution derived with a rake angle constraint of ±20°.

Acknowledgments
We thank the Caltech ARIA Team for providing the daily GNSS time series. We thank the GFZ for providing global gravity field models which can be downloaded at http://icgem.gfz-potsdam.de/ICGEM/. Moreover, we thank ESA for providing GOCE data through the GOCE Virtual Online Archive from ESA's website http://earth.esa.int. We are grateful to the Editor (Paul Tregoning) and three anonymous reviewers for their constructive comments which lead to a significant improvement of the manuscript.

References

Balmino, G., F. Perosanz, R. Rummel, N. Sneeuw, and H. Sunkel (1999), CHAMP, GRACE and GOCE: Mission concepts and simulations, *Boll. Geofis. Teor. Appl.*, *40*(3–4), 309–319.

Bertiger, W., S. D. Desai, B. Haines, N. Harvey, A. W. Moore, S. Owen, and J. P. Weiss (2010), Single receiver phase ambiguity resolution with GPS data, *J. Geod.*, *84*(5), 327–337.

Bettadpur, S., and the CSR Level-2 Team (2012), Assessment of GRACE mission performance and the RL05 gravity fields, paper G31C-02, presented at 2012 Fall Meeting, AGU, San Francisco, Calif., Dec.

Bletery, Q., A. Sladen, B. Delouis, M. Vallee, J. M. Nocquet, L. Rolland, and J. Jiang (2014), A detailed source model for the M_w 9.0 Tohoku-Oki earthquake reconciling geodesy, seismology and tsunami records, *J. Geophys. Res. Solid Earth*, *119*, 7636–7653, doi:10.1002/2014JB011261.

Bletery, Q., A. Sladen, B. Delouis, and L. Mattéo (2015), Quantification of tsunami bathymetry effect on finite fault slip inversion, *Pure Appl. Geophys.*, *172*, 3655–3670.

Bouman, J., and M. Fuchs (2012), GOCE gravity gradients vs. global gravity field models, *Geophys. J. Int.*, *189*(2), 846–850, doi:10.1111/j.1365-246X.2012.05428.x.

Bouman, J., S. Fiorot, M. Fuchs, T. Gruber, E. Schrama, C. C. Tscherning, M. Veicherts, and P. Visser (2011), GOCE gravitational gradients along the orbit, *J. Geod.*, *85*(11), 791–805, doi:10.1007/s00190-011-0464-0.

Bouman, J., M. Fuchs, V. Lieb, M. Oliveira, M. Schmidt, P. Visser, T. Broerse, and E. Schrama (2013), GOCE time variations STSE GOCE+, *Final Rep. GOCE/TH4/FR, Issue 2.*, Eur. Space Agency.

Bouman, J., et al. (2015), GOCE gravity gradient data for lithospheric modeling, *Int. J. Appl. Earth Observ. Geoinform.*, *35*(A), 16–30, doi:10.1016/j.jag.2013.11.001.

Broerse, T., P. Visser, J. Bouman, M. Fuchs, B. Vermeersen, and M. Schmidt (2011), Modelling and observing the M_w 8.8 Chile 2010 and M_w 9.0 Japan 2011 earthquakes using GOCE, in *Earth on the Edge: Science for a Sustainable Planet, ESA Publ. SP-696*, pp. 303–310, Springer, Berlin.

Broerse, T., R. Riva, and B. Vermeersen (2014), Ocean contribution to seismic gravity changes: The sea level equation for seismic perturbations revisited, *Geophys. J. Int.*, *199*(2), 1094–1109, doi:10.1093/gji/ggu315.

Broerse, T., R. Riva, W. Simons, R. Govers, and B. Vermeersen (2015), Postseismic GRACE and GPS observations indicate a rheology contrast above and below the Sumatra slab, *J. Geophys. Res. Solid Earth*, *120*, 5343–5361, doi:10.1002/2015JB011951.

Bruinsma, S., C. Foerste, O. Abrikosov, J.-C. Marty, M.-H. Rio, S. Mulet, and S. Bonvalot (2013), The new ESA satellite-only gravity field model via the direct approach, *Geophys. Res. Lett.*, *40*, 3607–3612, doi:10.1002/grl.50716.

Cambiotti, G., and R. Sabadini (2012), A source model for the great 2011 Tohoku earthquake (M_w = 9.1) from inversion of GRACE gravity data, *Earth Planet. Sci. Lett.*, *335*, 72–79.

Cambiotti, G., and R. Sabadini (2013), Gravitational seismology retrieving centroid-moment-tensor solution of the 2011 Tohoku earthquake, *J. Geophys. Res. Solid Earth*, *118*, 183–194, doi:10.1029/2012JB009555.

Cheng, M., and J. Ries (2014), GRACE Tech. Note 07, Center for Space Res., The Univ. of Tex. at Austin, Austin. [Available at ftp:/podaac.jpl.nasa.gov/allData/grace/docs/TN-07_C20_SLR.txt.]

Diao, F., X. Xiong, and Y. Zheng (2012), Static slip model of the M_w 9.0 Tohoku (Japan) earthquake: Results from joint inversion of terrestrial GPS data and seafloor GPS/acoustic data, *Chin. Sci. Bull.*, *57*(16), 1990–1997, doi:10.1007/s11434-012-5014-5.

Diao, F., X. Xiong, R. Wang, W. Zheng, T. R. Walter, H. Weng, and J. Li (2014), Overlapping post-seismic deformation processes: Afterslip and viscoelastic relaxation following the 2011 M_w 9.0 Tohoku (Japan) earthquake, *Geophys. J. Int.*, *196*(1), 218–229, doi:10.1093/gji/ggt376.

Ebbing, J., J. Bouman, M. Fuchs, V. Lieb, R. Haagmans, J. A. C. Meekes, and R. A. Fattah (2013), Advancements in satellite gravity gradient data for crustal studies, *Leading Edge*, *32*(8), 900–906, doi:10.1190/tle32080900.1. Society of Exploration Geophysicists.

European Space Agency (1999), *Gravity Field and Steady-State Ocean Circulation Mission, Report for Mission Selection of the Four Candidate Earth Explorer Missions*, ESA SP-1233(1), ESA Publ. Division, European Space Agency, Noordwijk, Netherlands.

Feng, G., and S. Jónsson (2012), Shortcomings of InSAR for studying megathrust earthquakes: The case of the M_w9.0 Tohoku-Oki earthquake, *Geophys. Res. Lett.*, *39*, L10305, doi:10.1029/2012GL051628.

Fuchs, M., and J. Bouman (2011), Rotation of GOCE gravity gradients to local frames, *Geophys. J. Int.*, *187*, 743–753, doi:10.1111/j.1365-246X.2011.05162.x.

Fuchs, M., J. Bouman, T. Broerse, P. Visser, and B. Vermeersen (2013), Observing coseismic gravity change from the Japan Tohoku-Oki 2011 earthquake with GOCE gravity gradiometry, *J. Geophys. Res. Solid Earth*, *118*, 5712–5721, doi:10.1002/jgrb.50381.

Fuchs, M., T. Broerse, A. Hooper, J. Pietrzak, and J. Bouman (2015), Grace gravity data to enhance the modeling of coseismic slip distribution for the 2011 Tohoku-Oki earthquake.

Fujiwara, T., S. Kodaira, T. No, Y. Kaiho, N. Takahashi, and Y. Kaneda (2011), The 2011 Tohoku-Oki earthquake: Displacement reaching the trench axis, *Science*, *334*(6060), 1240–1240.

Gou, F., I. Aki, K. Shuichi, T. Narumi, and K. Yoshiyuki (2006), Confirming sharp bending of the Pacific plate in the northern Japan trench subduction zone by applying a traveltime mapping method, *Phys. Earth. Planet Int.*, *157*, 72–85, doi:10.1016/j.pepi.2006.03.013.

Grombein, T., K. Seitz, and B. Heck (2011), Optimized formulas for the gravitational field of a tesseroid, *J. Geod.*, *87*(7), 645–660, doi:10.1007/s00190-013-0636-1.

Han, S. C., J. Sauber, and R. Riva (2011), Contribution of satellite gravimetry to understanding seismic source processes of the 2011 Tohoku-Oki earthquake, *Geophys. Res. Lett.*, *38*, L24312, doi:10.1029/2011GL049975.

Han, S. C., J. Sauber, and F. Pollitz (2014), Broadscale postseismic gravity change following the 2011 Tohoku-Oki earthquake and implication for deformation by viscoelastic relaxation and afterslip, *Geophys. Res. Lett.*, *41*, 5797–5805, doi:10.1002/2014GL060905.

Hoechner, A. (2010), GPS Based Analysis of Earthquake Induced Phenomena at the Sunda Arc. Institutional Repository of the University of Potsdam, Potsdam, Germany. [Available at http://opus.kobv.de/ubp/volltexte/2011/ 5316/.]

Hooper, A., B. Ófeigsson, F. Sigmundsson, B. Lund, P. Einarsson, H. Geirsson, and E. Sturkell (2011), Increased capture of magma in the crust promoted by icecap retreat in Iceland, *Nat. Geosci.*, *4*, 783–786, doi:10.1038/NGEO1269.

Hooper, A., et al. (2012), Importance of horizontal seafloor motion on tsunami height for the 2011 $M = 9.0$ Tohoku-Oki earthquake, *Earth Planet. Sci. Lett.*, *361*, 469–479.

Loveless, J. P., and B. J. Meade (2011), Spatial correlation of interseismic coupling and coseismic rupture extent of the 2011 $M_W = 9.0$ Tohoku-Oki earthquake, *Geophys. Res. Lett.*, *38*, L17306, doi:10.1029/2011GL048561.

Nishimura, T., H. Munekane, and H. Yarai (2011), The 2011 off the Pacific Coast of Tohoku earthquake and its aftershocks observed by GeoNet, *Earth Planets Space*, *63*, 631–636, doi:10.5047/eps.2011.06.025.

Matsuo, K., and K. Heki (2011), Coseismic gravity changes of the 2011 Tohoku-oki earthquake from satellite gravimetry, *Geophys. Res. Lett.*, *38*, L00G12, doi:10.1029/2011GL049018.

Mayer-Guerr, T., et al. (2012), The new combined satellite only model GOCO03s, Poster presented at the GGHS2012, Venice, Italy.

Mosegaard, K., and A. Tarantola (1995), Monte Carlo sampling of solutions to inverse problems, *J. Geophys. Res.*, *100*, 12,431–12,447.

Ozawa, S., T. Nishimura, H. Munekata, H. Suito, T. Kobayashi, M. Tobita, and T. Imakiire (2012), Preceding, coseismic, and postseismic slips of the 2011 Tohoku earthquake, Japan, *J. Geophys. Res.*, *117*, B07404, doi:10.1029/2011JB009120.

Pail, R., et al. (2011), First GOCE gravity field models derived by three different approaches, *J. Geod.*, *85*, 819–843, doi:10.1007/s00190-011-0467-x.

Rebischung, P., J. Griffiths, J. Ray, R. Schmid, X. Collilieux, and B. Garayt (2012), IGS08: The IGS realization of ITRF2008, *GPS Solut.*, *16*, 483–494, doi:10.1007/s10291-011-0248-2.

Rodell, M., et al. (2004), The Global Land Data Assimilation System, *Bull. Am. Meteorol. Soc.*, *85*(3), 381–394.

Sabadini, R., and B. Vermeersen (2014), *Global Dynamics of the Earth: Applications of Normal Mode Relaxation Theory to Solid-Earth Geophysics*, Kluwer Acad., Dordrecht, Netherlands.

Satake, K., K. Shimazaki, Y. Tsuji, and K. Ueda (1996), Time and size of a giant earthquake in Cascadia inferred from Japanese tsunami records of January 1700, *Nature*, *379*, 246–249.

Schwatke, C., W. Bosch, R. Savcenko, and D. Dettmering (2010), OpenADB—An open database for multi-mission altimetry, presented at the EGU 2010 as a Poster, Vienna, Austria.

Sun, T., et al. (2014), Prevalence of viscoelastic relaxation after the 2011 Tohoku-Oki earthquake, *Nature*, *514*, 84–87, doi:10.1038/nature1377.

Sweanson, S., and J. Wahr (2006), Post processing removal of correlated errors in GRACE data, *Geophys. Res. Lett.*, *33*, L08402, doi:10.1029/2005GL025285.

Tapley, B. D., S. Bettadpur, M. Watkins, and C. Reigber (2004), The gravity recovery and climate experiment: Mission overview and early results, *Geophys. Res. Lett.*, *31*, L09607, doi:10.1029/2004GL019920.

Tarantola, A. (2005), *Inverse Problem Theory and Methods for Model Parameter Estimation*, 36 pp., SIAM, Philadelphia, Pa.

U.S. Geological Survey (2014), U.S. Geological Survey (and Supporting Agencies), 2006. Quaternary fault and fold database, year of access 2014, from USGS web site: http://earthquakes.usgs.gov/.

Wang, L., C. K. Shum, F. J. Simons, B. Tapley, and C. Dai (2012), Coseismic and postseismic deformation of the 2011 Tohoku-Oki earthquake constrained by GRACE gravimetry, *Geophys. Res. Lett.*, *39*, L07301, doi:10.1029/2012GL051104.

Yamagiwa, S., S. Miyazaki, K. Hirahara, and Y. Fukahata (2015), Afterslip and viscoelastic relaxation following the 2011 Tohoku-Oki earthquake (M_w9.0) inferred from inland GPS and seafloor GPS/Acoustic data, *Geophys. Res. Lett.*, *42*, 66–73, doi:10.1002/2014GL061735.

Zhou, X., G. Cambiotti, W. Sun, and R. Sabadini (2014), The coseismic slip distribution of a shallow subduction fault constrained by prior information: The example of 2011 Tohoku (M_w 9.0) megathrust earthquake, *Geophys. J. Int.*, *199*, 981–995, doi:10.1093/gji/ggu310.

Zumberge, J. F., M. B. Heflin, D. C. Jefferson, M. M. Watkins, and F. H. Webb (1997), Precise point positioning for the efficient and robust analysis of GPS data from large networks, *J. Geophys. Res.*, *102*(B3), 5005–5017.